Journal of ELECTRONIC MATERIALS, Vol. 46, No. 8, 2017
DOI: 10.1007/s11664-017-5417-9

KH_2PO_4-Assisted Synthesis and Electrochemical Performance of Highly Uniform $CuBi_2O_4$ Microspheres Hierarchically Self-Assembled by Nanoparticles

FEI WANG,[1] HUA YANG,[1,2] YUNCHUAN ZHANG,[1] and HAIMIN ZHANG[1]

1.—School of Science, Lanzhou University of Technology, Lanzhou 730050, China. 2.—e-mail: hyang@lut.cn

The effect of KH_2PO_4 on the synthesis of $CuBi_2O_4$ microstructures was investigated. The samples were characterized by powder x-ray diffraction (XRD), scanning electron microscopy (SEM), Brunauer–Emmett–Teller (BET) analysis, x-ray photoelectron spectroscopy (XPS) and ultraviolet (UV)-visible diffuse reflectance spectroscopy. It is demonstrated that the use of KH_2PO_4 leads to the production of highly uniform $CuBi_2O_4$ microspheres hierarchically self-assembled by nanoparticles. With increasing the KH_2PO_4 concentration from 0.5 M to 1.4 M, the average diameter of the resultant microspheres decreases gradually from 3.3 μm to 1.4 μm. However, further increase in the KH_2PO_4 concentration up to 1.5 M leads to a sudden increase in the average diameter of the resultant microspheres up to 2.3 μm. In addition, a minor amount of bamboo leaf- or pine needle-like structures are visible in the samples prepared at the KH_2PO_4 concentrations of 1.0–1.5 M. The bandgap energy of the as-prepared samples is measured to be 1.89 eV by UV-visible diffuse reflectance spectroscopy. The electrochemical performance of the samples was investigated by cyclic voltammetry, galvanostatic charge-discharge measurements, and electrochemical impedance spectroscopy in 2 M KOH electrolyte. Among the hierarchical microspheres, those prepared at the KH_2PO_4 concentration of 1.4 M deliver a relatively higher specific capacitance due to their smaller size (1284 F g^{-1} at a current density of 2 A g^{-1}).

Key words: $CuBi_2O_4$, self-assembled hierarchical microspheres, KH_2PO_4, electrochemical performance

INTRODUCTION

Three dimensional (3D) self-assembled hierarchical architectures have received a great deal of attention over the years since they exhibit many unique properties.[1–7] For example, due to enhanced light trapping by multiple scattering, they usually show a superior light absorption efficiency compared with other structures like solid particles. This makes 3D self-assembled hierarchical architectures particularly interesting as photocatalysts—e.g., flower-like hierarchical Bi_2WO_6 microspheres were demonstrated to exhibit much higher photocatalytic activity than Bi_2WO_6 nanoparticles.[5] 3D self-assembled hierarchical architectures have also been widely applied to supercapacitor electrodes.[6,7] It is expected to deliver an enhanced specific capacitance per unit surface area of the electrode because of the increase in charge diffusion to inner active sites.

Recently, copper bismuth oxide ($CuBi_2O_4$) has been extensively studied as an important functional material. This oxide has a spinel-type structure with square planar CuO_4 groups linked to distorted trigonal BiO_6 polyhedra,[8] and possesses many promising physicochemical properties including magneticity, dielectricity, high-temperature heat capacity, photoelectrochemical property, optical property, photocatalysis, and electrochemical

(Received September 13, 2016; accepted February 24, 2017; published online March 9, 2017)

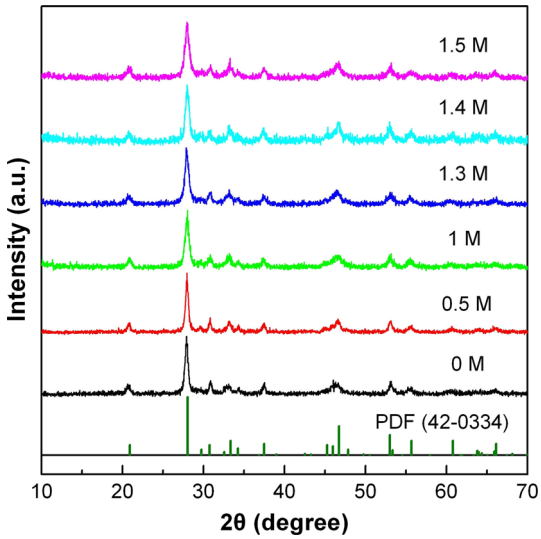

Fig. 1. XRD patterns of $CuBi_2O_4$ samples prepared at different KH_2PO_4 contents, along with the standard XRD line pattern for $CuBi_2O_4$ tetragonal structure (PDF card no. 42-0334).

capacitance.[9–18] In particular, it was demonstrated that $CuBi_2O_4$ exhibits a good pseudocapacitive behavior and can deliver a specific capacitance up to 1895 F g^{-1} in a KOH electrolyte, which is larger than that for most transition metal oxides.[18] The excellent electrochemical performance makes $CuBi_2O_4$ attractive for the application as supercapacitor electrode material. To address the morphology-mediated tailoring of the performance of $CuBi_2O_4$, considerable recent efforts have been made to fabricate 3D self-assembled hierarchical $CuBi_2O_4$ architectures such as hierarchical nanoflowers, hedgehog-like hierarchical microspheres, sphere-like hierarchical architectures built from nanorod arrays, and micro-sphere structures comprised of nanometer quadrilateral plates.[19–23] The hydrothermal process is the most commonly used method to synthesize the self-assembled hierarchical $CuBi_2O_4$ architectures; however, it requires power consumption to drive the hydrothermal reaction. The coprecipitation method is an alternative method exhibiting the capability to create 3D self-assembled hierarchical architectures without energy consumption. In this paper, we report the synthesis of highly uniform $CuBi_2O_4$ microspheres hierarchically self-assembled by nanoparticles based on a coprecipitation route with the aid of KH_2PO_4. The electrochemical capacitance of the as-prepared samples was investigated.

EXPERIMENTAL

All raw materials and chemical reagents used in this study are of analytical grade without further purification. 1.9402 g (0.004 mol) of $Bi(NO_3)_3{\cdot}5H_2O$, 0.4832 g (0.002 mol) of $Cu(NO_3)_2{\cdot}3H_2O$ and a certain amount of KH_2PO_4 were successively dissolved in 20 mL of dilute nitric acid solution (2.4 mol L^{-1})

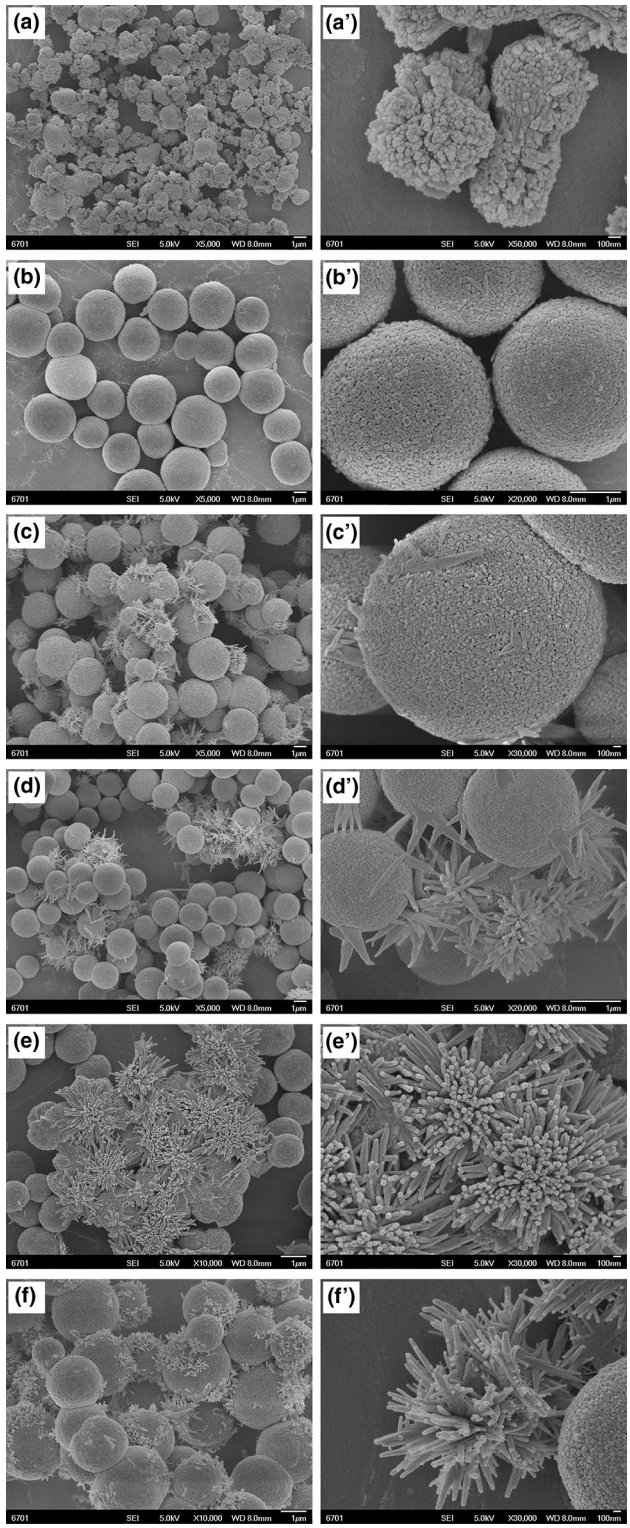

Fig. 2. SEM images of $CuBi_2O_4$ samples prepared at different KH_2PO_4 contents. (a)-(a′) 0 M (in the absence of KH_2PO_4); (b)-(b′) 0.5 M; (c)-(c′) 1.0 M; (d)-(d′) 1.3 M; (e)-(e′) 1.4 M; (f)-(f′) 1.5 M.

under magnetic stirring, and the resultant mixture was designated as solution A. 12.8 g of NaOH was dissolved in 60 mL of distilled water, which was designated as solution B. Solution B was slowly

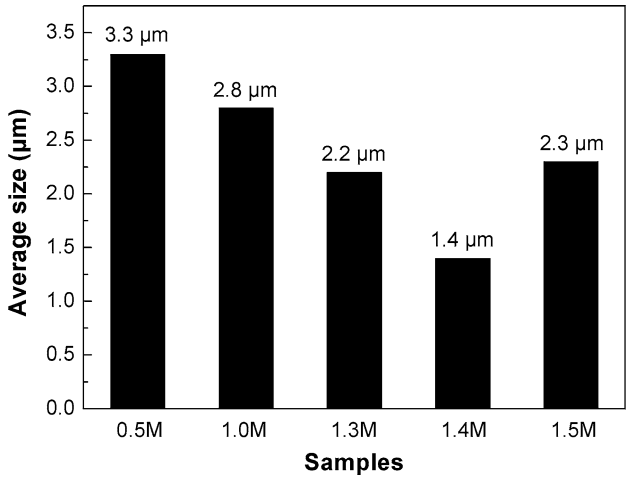

Fig. 3. Average microsphere diameter of the samples prepared at different KH_2PO_4 contents.

added to solution A drop by drop under constant stirring, and a suspension solution was immediately formed. The suspension was continuously stirred with a magnetic stirring bar for 12 h, during which a brown precipitate was gradually formed. The reaction system was maintained at a temperature of 15°C by means of an external ice-water bath. The precipitate was collected and washed using distilled water and ethanol for 5 times, and then submitted to drying in a thermostatic drying oven at 60°C for 12 h to obtain final $CuBi_2O_4$ product. By varying the content of KH_2PO_4 from 0 mol L^{-1} to 1.5 mol L^{-1} (M; concentration in final reaction solution), we prepared a series of $CuBi_2O_4$ samples.

The phase purity of the as-prepared $CuBi_2O_4$ samples was examined by using powder x-ray diffraction (XRD) with Cu Kα radiation. The morphology of the samples was investigated by using field-emission scanning electron microscopy (SEM). The ultraviolet (UV)-visible diffuse reflectance spectrum of the samples was measured on an UV-visible spectrophotometer with an integrating sphere attachment by using $BaSO_4$ as the reference. The Brunauer–Emmett–Teller (BET) specific surface area of the samples was measured by the N_2 adsorption/desorption technique on an ASAP20 20 M system. The chemical composition and electron binding energies for the elements were measured by x-ray photoelectron spectroscopy (XPS) on a PHI-5702 multifunctional x-ray photoelectron spectrometer. The binding energy scale of the XPS data was calibrated against the adventitious C 1s peak at the binding energy of 284.8 eV.

The electrochemical capacitance of $CuBi_2O_4$ samples was measured on a CST 350 electrochemical workstation using a three-electrode cell configuration which includes the counter electrode (a platinum foil), reference electrode (a standard calomel electrode) and working electrode. The working electrode was prepared as follows. 1 mg of $CuBi_2O_4$, 0.125 mg of carbon black and 0.125 mg of polyvinylidene fluoride (PVDF) were mixed together using 1-methyl-2-pyrrolidione (NMP) as solvent to form a slurry. The slurry was uniformly coated onto a Ni foam electrode with an area of 1 cm^2, and was then dried at 60°C for 12 h in a thermostat drying oven. KOH aqueous solution with a concentration of 2 M was used as the electrolyte.

RESULTS AND DISCUSSION

Figure 1 shows the XRD patterns of $CuBi_2O_4$ samples prepared at different KH_2PO_4 contents, along with the standard XRD line pattern for $CuBi_2O_4$ tetragonal structure (PDF card no. 42-0334). It is seen that for all the samples, the diffraction peaks are in good agreement with those in the PDF standard card, and no diffraction peaks assignable to other secondary phases are detected. This indicates that the as-synthesized $CuBi_2O_4$ samples crystallize in a pure tetragonal phase.

Figure 2 shows the SEM images of $CuBi_2O_4$ samples prepared at different KH_2PO_4 contents. It is seen that, in the absence of KH_2PO_4, the prepared sample is composed of nonuniform and irregular cauliflower-like microstructures (Fig. 2a-a′). The cauliflower-like microstructures are constructed from nanoparticles with a diameter of several tens of nanometers. When KH_2PO_4 is introduced into the precursor solution, it brings about the formation of regular and uniform hierarchical microspheres assembled by nanoparticles with several tens of nanometers in size. Among the resultant samples, the one prepared at the KH_2PO_4 concentration of 0.5 M consists of bare microspheres without the presence of other morphologies (Fig. 2b-b′), while those prepared at the KH_2PO_4 concentrations of 1.0–1.5 M contain, besides the main microspheres, a minor amount of bamboo leaf- or pine needle-like structures (Fig. 2c-f′). The average microsphere diameter of the samples is shown in Fig. 3. With increasing the KH_2PO_4 concentration from 0.5 M to 1.4 M, the average diameter of the resultant microspheres decreases gradually from 3.3 μm to 1.4 μm. However, when the KH_2PO_4 concentration is further increased up to 1.5 M, the obtained microspheres exhibit a sudden increase in the average diameter up to 2.3 μm. We speculate that the surface energy of the freshly formed $CuBi_2O_4$ nanocrystals could be increased after 1.5 M KH_2PO_4, and thus they tend to assemble into large microspheres. The BET specific surface area of the samples prepared at the KH_2PO_4 concentrations of 0 M, 0.5 M, 1.0 M, 1.3 M, 1.4 M, and 1.5 M is measured by the N_2 adsorption/desorption technique as 17.9 m^2 g^{-1}, 5.3 m^2 g^{-1}, 7.6 m^2 g^{-1}, 10.3 m^2 g^{-1}, 14.8 m^2 g^{-1}, and 9.1 m^2 g^{-1}, respectively.

In order to elucidate the growth process of hierarchical $CuBi_2O_4$ microspheres, we monitored the products reacted for different times at the

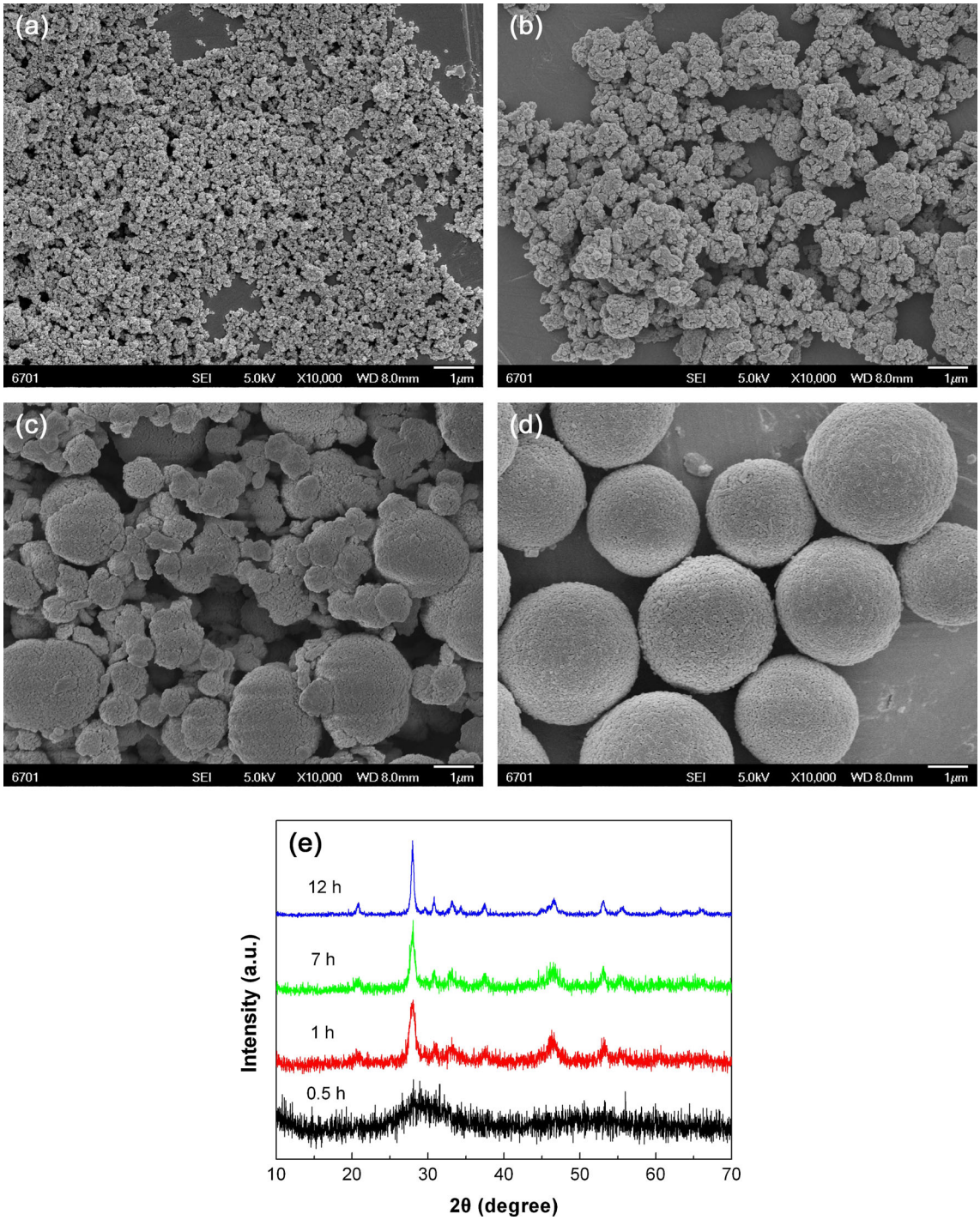

Fig. 4. SEM images of $CuBi_2O_4$ samples obtained at different reaction times of (a) 0.5 h, (b) 1 h, (c) 7 h, and (d) 12 h (KH_2PO_4 concentration: 0.5 M). (e) The corresponding XRD patterns of the samples obtained at different reaction times.

KH_2PO_4 concentration of 0.5 M. Figure 4a and d show the SEM images of the samples obtained at 0.5 h, 1 h, 7 h, and 12 h, respectively. The corresponding XRD patterns of the samples are shown in Fig. 4e. At the initial stage of the reaction, ultrafine powders are formed, which are characterized to be amorphous $Cu(OH)_2$ and $Bi(OH)_3$ precipitates. After 1 h of reaction, the amorphous precipitates are crystallized into $CuBi_2O_4$ nanocrystals. With prolonging the reaction time, the formed $CuBi_2O_4$ nanocrystals assemble into hierarchical architectures. The SEM image of the product at 7 h of reaction demonstrates the formation of hierarchical microspheres, but these microspheres are

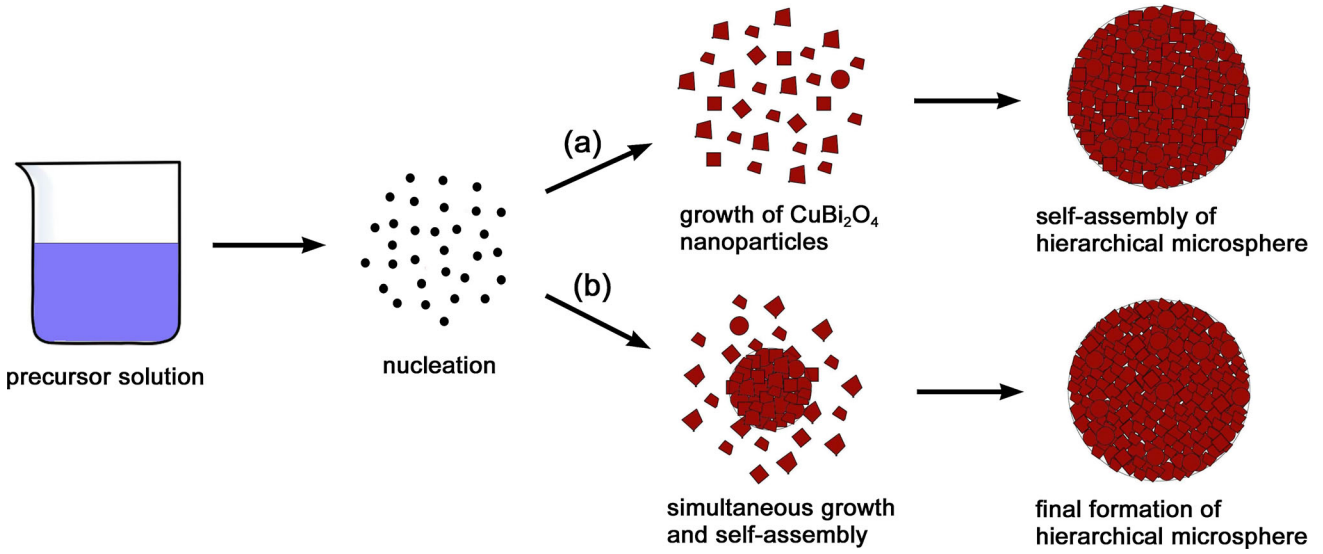

Fig. 5. Schematic illustration of the formation process of $CuBi_2O_4$ hierarchical microspheres. (a) First growth of $CuBi_2O_4$ nanoparticles and then self-assembly of hierarchical microspheres. (b) Simultaneous growth of $CuBi_2O_4$ nanoparticles and self-assembly of hierarchical microspheres.

nonuniform aggregates of $CuBi_2O_4$ nanocrystals. When the reaction time is increased up to 12 h, regular and uniform hierarchical microspheres are formed.

The formation mechanism of hierarchical $CuBi_2O_4$ microspheres can be simply described as follows. When NaOH solution is added to the Cu^{2+}/Bi^{3+}-containing reaction system, amorphous $Cu(OH)_2$ and $Bi(OH)_3$ precipitates are produced immediately. These hydroxides undergo an attack of the mineralizer NaOH to dissolve and form ion groups. In the region of supersaturated fluid, $CuBi_2O_4$ nuclei are formed and grow into nanocrystals. To reduce the overall surface energy, the freshly formed $CuBi_2O_4$ nanocrystals self-assemble into hierarchical architectures. The nucleation, growth and self-assembly processes could proceed simultaneously. When KH_2PO_4 is introduced into the reaction system, the nucleation and growth rates could become slow. Slower nucleation and growth kinetics tend to favour isotropic growth,[22] consequently leading to the easy formation of spherical, polyhedral, or cubic particles. These particles have isotropic surface energy and tend to self-assemble into regular and uniform hierarchical microspheres. The schematic illustration of the forming process of hierarchical $CuBi_2O_4$ microspheres is presented in Fig. 5. It is also noted that the nucleation and growth rates could become very fast in some local regions due to the ion accumulation, thus resulting in the formation of minor amounts of bamboo leaf- or pine needle-like structures.

Figure 6 shows the UV-visible diffuse reflectance spectra of $CuBi_2O_4$ samples and the corresponding first derivative spectra. The peak wavelength in the first derivative spectra is characterized to be the absorption edge of the samples. It is seen that all the samples have a similar absorption edge at around 657 nm and this absorption edge is attributed to the electron transition from the valence band to the conduction band, from which the bandgap energy E_g of the samples is obtained to be 1.89 eV.

We also investigated the elemental oxidation state of $CuBi_2O_4$ hierarchical microspheres prepared at the KH_2PO_4 concentration of 0.5 M and cauliflower-like architectures prepared in the absence of KH_2PO_4. Figure 7a shows the XPS survey spectra of the two samples, revealing the presence of the elements Cu, Bi and O. Figure 7b and d show the XPS spectra of Bi 4f, Cu 2*p* and O 1s, respectively. The XPS signals of the two samples are seen to be very similar, suggesting that $CuBi_2O_4$ with microspherical and cauliflower-like architectures has the same elemental oxidation state. In Fig. 7b, the spectra present two sharp peaks at 158.7 eV and 163.9 eV, which correspond to the binding energies of Bi $4f_{7/2}$ and Bi $4f_{5/2}$, respectively. This implies that Bi exists in the +3 oxidation state.[24] On the spectra shown in Fig. 7c, the peaks at 933.9 eV and 953.8 eV are assigned to the binding energies for Cu $2p_{3/2}$ and Cu $2p_{1/2}$, respectively, and the peaks at 942.4 eV and 962.5 eV are characterized to be the satellite peaks of Cu 2*p*. The Cu 2*p* peak positions and the presence of satellite peaks confirm that the existence of the copper species in Cu^{2+} valence state. The O 1s XPS signals shown in Fig. 7d can be fitted into three peaks at 529.6 eV, 531.3 eV, and 532.9 eV. The main peak at 529.6 eV is attributed to the contribution of the crystal lattice oxygen. The exact assignment of the peaks at higher binding energies is rather complex and controversial since many factors (e.g., surface defects, chemisorbed oxygen species, water molecules, contaminants) could result in the appearance of the shoulder peaks.[25]

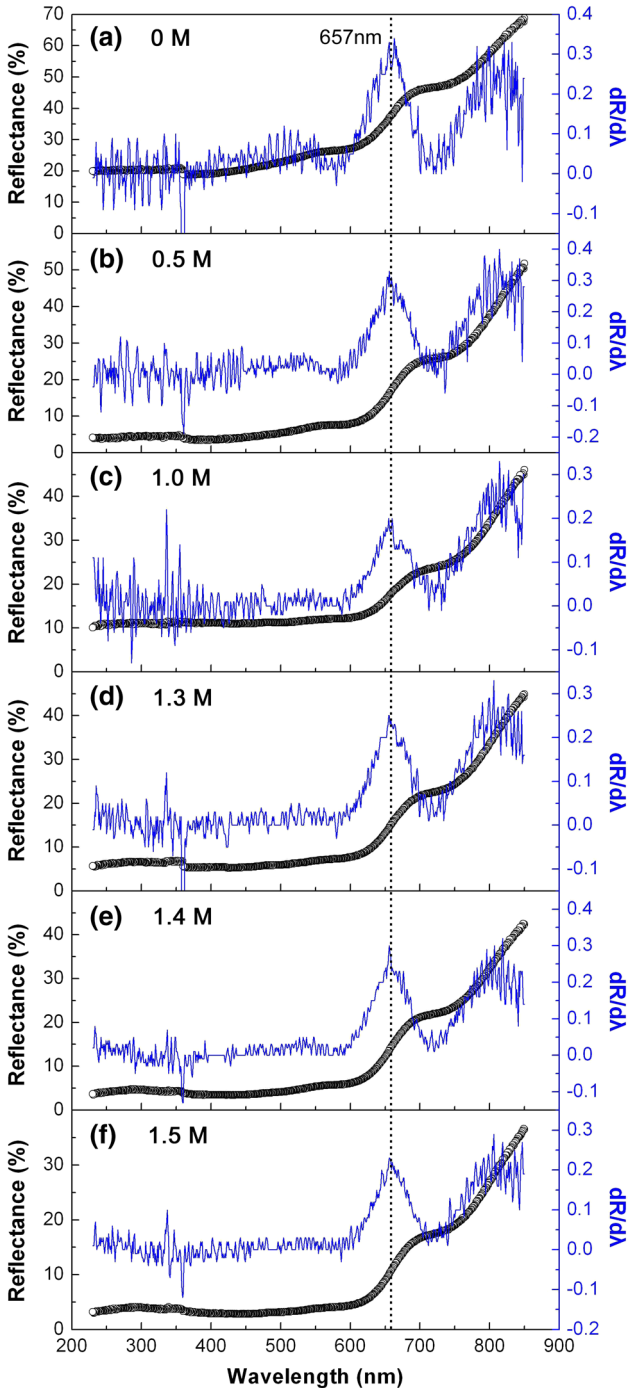

Fig. 6. UV-visible diffuse reflectance spectra of $CuBi_2O_4$ samples prepared at different KH_2PO_4 contents and the corresponding first derivative spectra. (a) 0 M; (b) 0.5 M; (c) 1.0 M; (d) 1.3 M; (e) 1.4 M; (f) 1.5 M.

Figure 8 shows the cyclic voltammetry (CV) curves of $CuBi_2O_4$ samples at various scan rates ranging from 5 mv s^{-1} to 25 mv s^{-1} over the potential window between −1.0 V and 0 V. It is seen that the CV curves for all the samples present a reduction peak R and two oxidation peaks O_1 and O_2, which arise due to the oxidation and reduction reactions taking place in $CuBi_2O_4$. Moreover, the reduction and oxidation potentials undergo a slight shift in negative and positive direction with increase in the scan rate, respectively. The CV curves elucidate a fast reversible redox reaction and a good pseudocapacitive behavior of $CuBi_2O_4$. It is noted that the CV curves are very similar to those of Bi-based oxides (e.g., Bi_2O_6[26] and Bi_2WO_6[27]), but not to those of Cu-based oxides (e.g., CuO[28] and $CuFe_2O_4$[29]). This implies that the oxidation state of bismuth plays the dominant role in the electrochemical mechanism. According to the redox mechanism described in the literatures,[26,30] the first step of the reduction process involves a partial dissolution of $CuBi_2O_4$ into the ionic species BiO^{2-}. The reduction peak R originates from the reduction of Bi(III) to Bi metal, while the oxidation peak O_2 arises from the oxidation of Bi metal to Bi(III). The small oxidation peak O_1 could be attributed to a small fraction of Bi metal sites located near the Bi-metal/micropore solution interface.[26]

Figure 9a-f show the charge-discharge curves of $CuBi_2O_4$ samples at various current densities ranging from 2 A g^{-1} to 12 A g^{-1} in the voltage window between 0 V and −1.0 V. It is seen that the curves exhibit non-linear behavior with a charge voltage plateau at around −0.5 V and a discharge voltage plateau at around −0.7 V. The non-linear characteristic of the charge-discharge curves suggests that the electrochemical reaction takes place due to the reversible redox process between the Bi(III) oxidation state and Bi^0 metallic state. The specific capacitance (C) of the samples can be calculated using the following equation

$$C = \frac{It}{m\Delta V} \quad (1)$$

where C, I, t, m, and ΔV are the specific capacitance (F g^{-1}) of the samples, the discharging current (A), the discharging time (s), the mass of $CuBi_2O_4$ (g), and the discharging potential range (V), respectively. The specific capacitance values of the samples calculated from their charge-discharge curves are shown in Fig. 9g. All the samples deliver an excellent specific capacitance above 900 F g^{-1}. Among the 5 types of hierarchical $CuBi_2O_4$ microspheres, the hierarchical microspheres prepared at the KH_2PO_4 concentration of 1.4 M exhibit the highest specific capacitance, reaching about 1284 F g^{-1} at current density of 2 A g^{-1}, and this value is very close to that of the cauliflower-like $CuBi_2O_4$ structures prepared in the absence of KH_2PO_4 (1290 F g^{-1}). This can be explained by the fact that the hierarchical microspheres prepared at the KH_2PO_4 concentration of 1.4 M have a relatively smaller size and thus can provide more available surface active sites for the electrochemical reaction. In addition, the specific capacitance of the samples is seen to decrease slightly with increasing the current density, which could be due to an increase in ionic

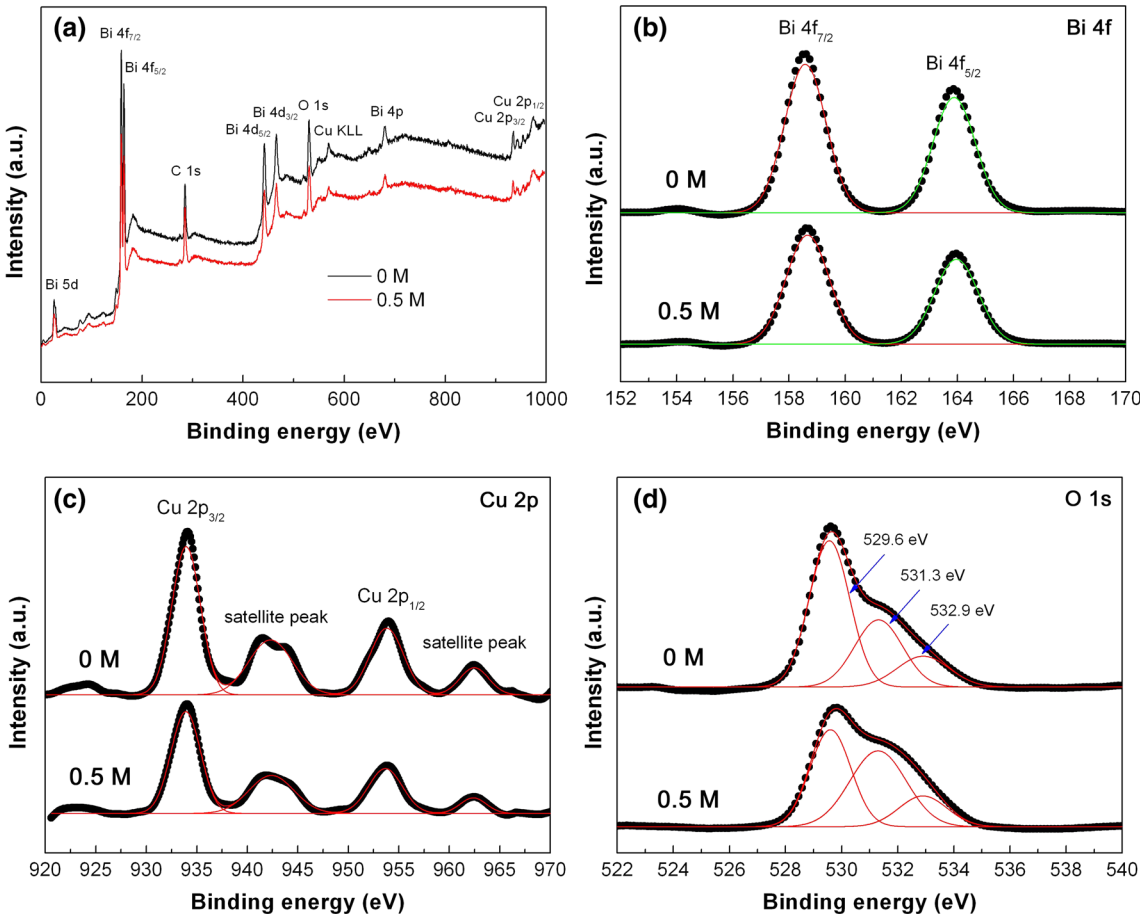

Fig. 7. XPS spectra of $CuBi_2O_4$ hierarchical microspheres prepared at the KH_2PO_4 concentration of 0.5 M and cauliflower-like architectures prepared in the absence of KH_2PO_4. (a) XPS survey spectra. (b) XPS spectra of Bi 4f. (c) XPS spectra of Cu 2p. (d) XPS spectra of O 1s.

resistivity and a decrease in charge diffusion to inner active sites and the redox reaction rate.[31]

The electrochemical cycling stability of $CuBi_2O_4$ samples was evaluated by the repeated charge-discharge measurement at a constant current density of 6 A g^{-1}. Figure 10 shows the capacitance retention as a function of the charge-discharge cycling number. The initial specific capacitance of $CuBi_2O_4$ samples prepared at KH_2PO_4 concentrations of 0 M, 0.5 M, 1.0 M, 1.3 M, 1.4 M, and 1.5 M is observed to be 1040 F g^{-1}, 930 F g^{-1}, 954 F g^{-1}, 970 F g^{-1}, 1069 F g^{-1}, and 1001 F g^{-1}, respectively. After 500 cycles, the specific capacitance of the samples is obtained as 799 F g^{-1}, 677 F g^{-1}, 755 F g^{-1}, 784 F g^{-1}, 884 F g^{-1}, and 776 F g^{-1}, maintaining 77%, 73%, 79%, 81%, 83%, and 78% of the initial capacitance, respectively.

Figure 11 shows the Nyquist plots of the impedance spectra for $CuBi_2O_4$ samples measured in the frequency range from 10^{-2} Hz to 10^5 Hz. Generally, Nyquist plots can be divided into two parts, i.e., a semicircle at the high-frequency region and a straight line in the low-frequency region. The semicircle at the high-frequency region is ascribed to the charge-transfer resistance at the electrode/electrolyte interface (i.e., faradic resistance), and the straight line in the low-frequency region is related to the diffusion of the electrolyte ions into/from the electrode pores.[32] On the Nyquist plots for all the $CuBi_2O_4$ samples, a very small semicircle is observed at the high-frequency region, implying that the charge-transfer resistance is very small. A small charge-transfer resistance means that the electrochemical reaction is easy to proceed with a high reversibility. In the low-frequency region, the phase angle for the Nyquist plots is seen to be much higher than 45°, which suggests an important capacitive behavior for $CuBi_2O_4$ samples.

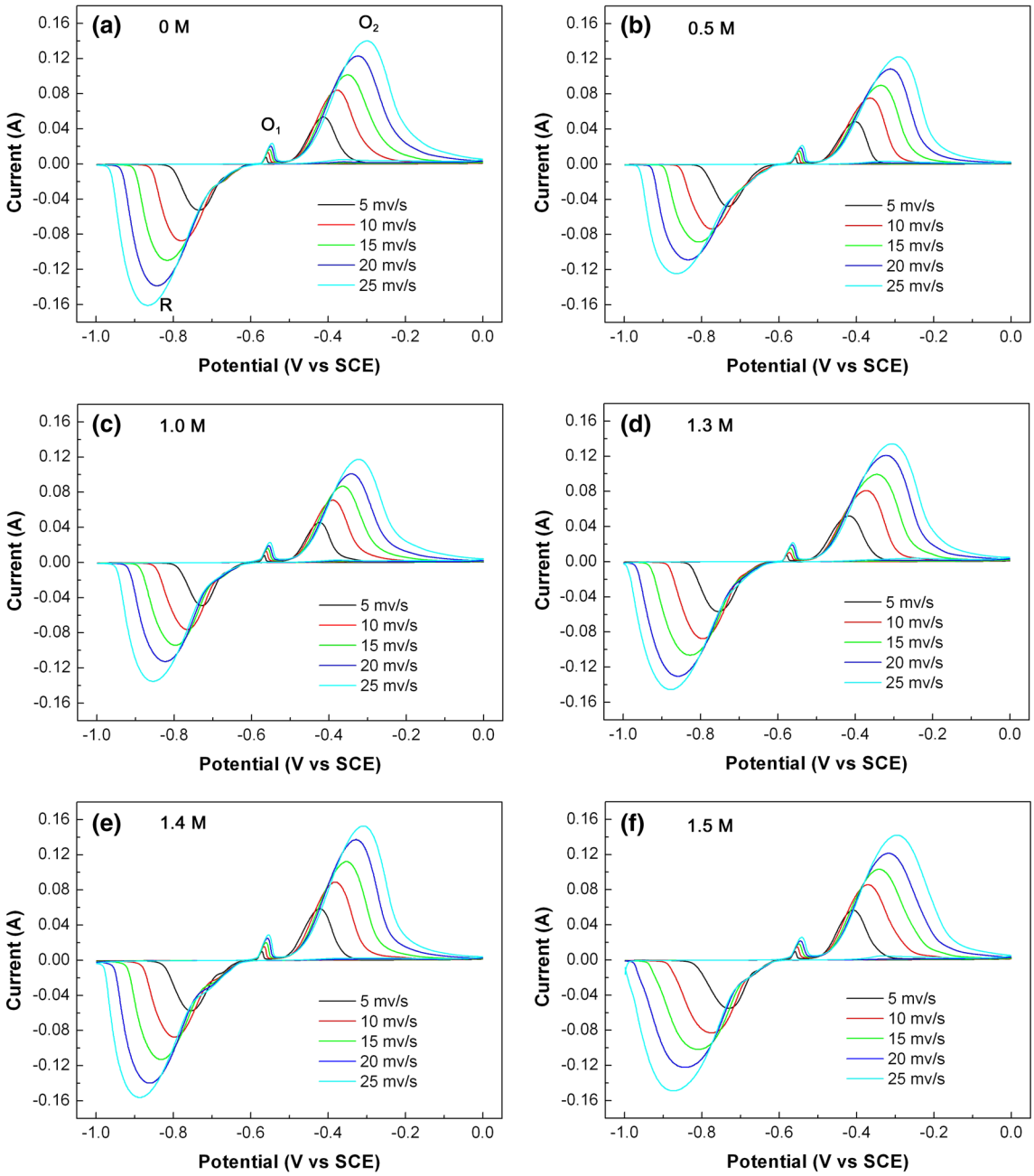

Fig. 8. CV curves of $CuBi_2O_4$ samples prepared at different KH_2PO_4 concentrations. (a) 0 M; (b) 0.5 M; (c) 1.0 M; (d) 1.3 M; (e) 1.4 M; (f) 1.5 M.

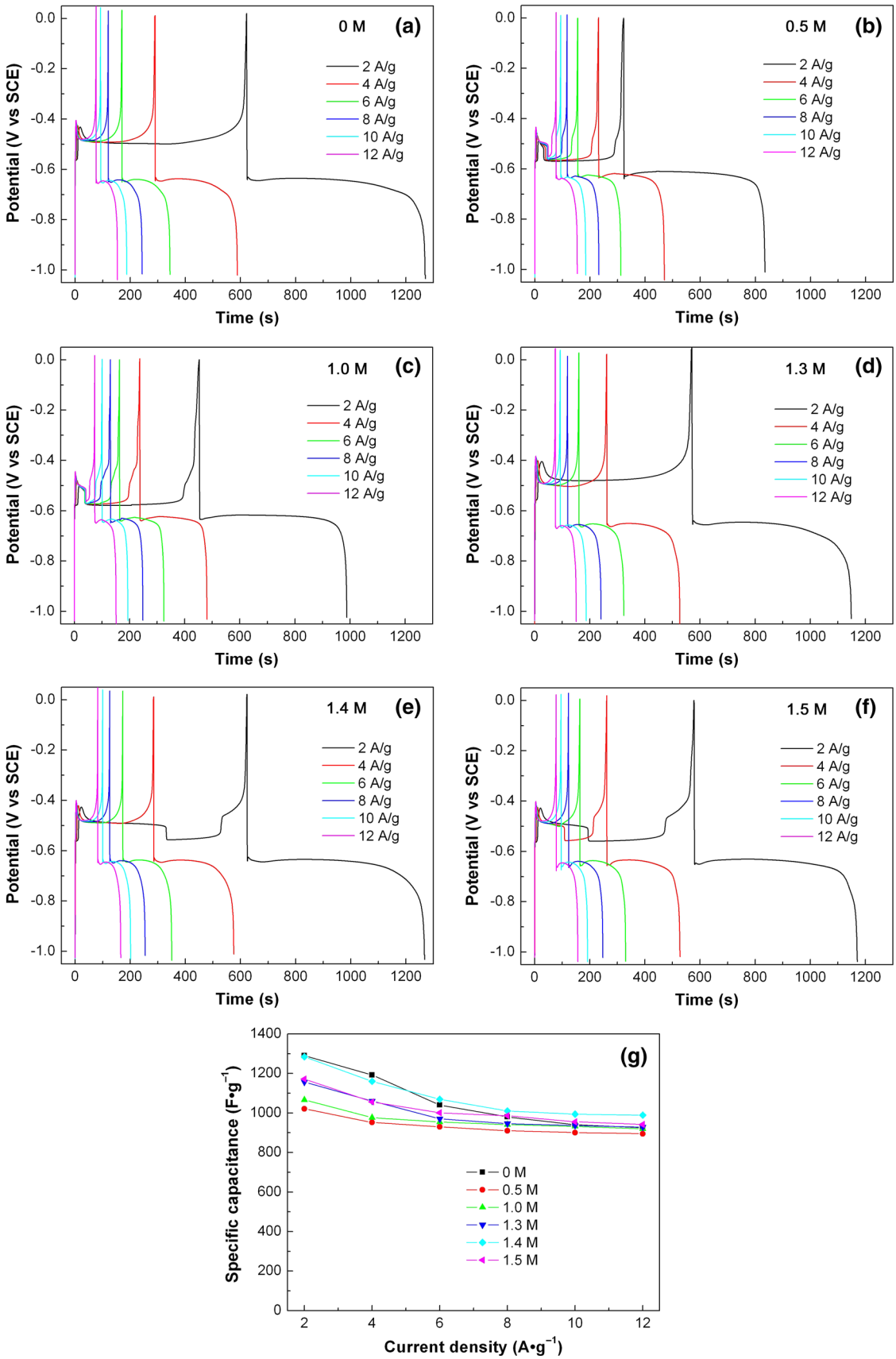

Fig. 9. Charge-discharge curves of $CuBi_2O_4$ samples prepared at different KH_2PO_4 concentrations of (a) 0 M, (b) 0.5 M, (c) 1.0 M, (d) 1.3 M, (e) 1.4 M and (f) 1.5 M. (g) Specific capacitance values of $CuBi_2O_4$ samples at various current densities.

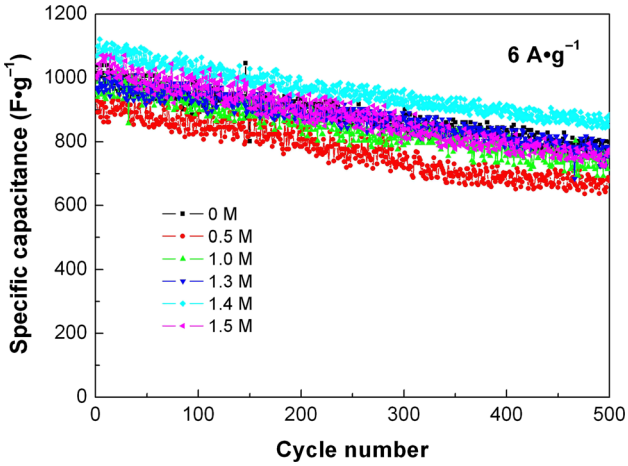

Fig. 10. Capacitance retention as a function of the charge-discharge cycling number at a constant current density of 6 A g^{-1}.

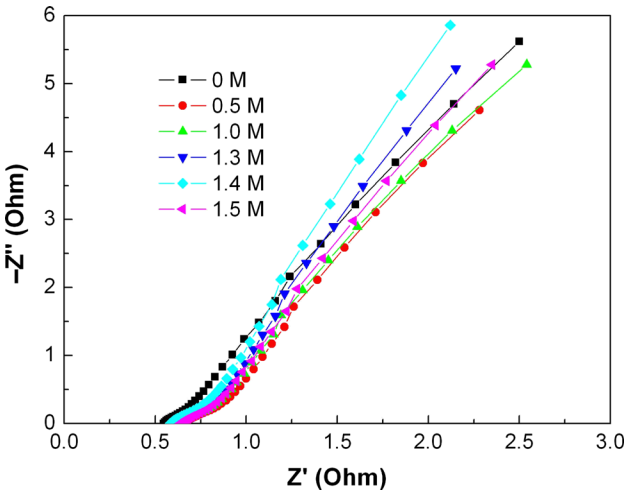

Fig. 11. Nyquist plots of the impedance spectra for $CuBi_2O_4$ samples.

CONCLUSIONS

Highly uniform $CuBi_2O_4$ microspheres hierarchically self-assembled by nanoparticles are prepared with the aid of KH_2PO_4. By varying the KH_2PO_4 concentration to be 0.5 M, 1.0 M, 1.3 M, 1.4 M, and 1.5 M, a series of hierarchical $CuBi_2O_4$ microspheres with average diameter of 3.3 μm, 2.8 μm, 2.2 μm, 1.4 μm, and 2.3 μm are obtained, respectively. In addition, a minor amount of bamboo leaf- or pine needle-like structures are visible in the latter four samples. UV-visible diffuse reflectance spectroscopy measurement shows that the as-prepared $CuBi_2O_4$ samples have a similar bandgap energy of 1.89 eV. Electrochemical test reveals that the samples exhibit a good electrochemical capacitance performance. The hierarchical microspheres prepared at the KH_2PO_4 concentration of 1.4 M deliver a relatively higher specific capacitance due to their smaller size, reaching 1284 F g^{-1} in 2 M KOH electrolyte at a current density of 2 A g^{-1}.

ACKNOWLEDGEMENTS

This work was supported by the National Natural Science Foundation of China (Grant Nos. 51262018 and 51662027).

REFERENCES

1. B. Bhowmik, V. Manjuladevi, R.K. Gupta, and P. Bhattacharyya, *IEEE Sens. J.* 16, 3488 (2016).
2. L.J. Di, H. Yang, T. Xian, R.S. Li, Y.C. Feng, and W.J. Feng, *Ceram. Int.* 40, 4575 (2014).
3. S. Kumar, T. Surendar, and V. Shanker, *Mater. Lett.* 123, 172 (2014).
4. S.W. Duo, Y.Y. Li, H. Zhang, T.Z. Liu, K. Wu, and Z.Q. Li, *Mater. Charact.* 114, 185 (2016).
5. Z.M. Cui, H. Yang, B. Wang, R.S. Li, and X.X. Wang, *Nanoscale Res. Lett.* 11, 190 (2016).
6. M.S. Javed, S.G. Dai, M.J. Wang, D.L. Guo, L. Chen, X. Wang, C. Hu, and Y. Xi, *J. Power Sources* 285, 63 (2015).
7. J. Ye, Z. Li, Z. Dai, Z.Y. Zhang, M.Q. Guo, and X.J. Wang, *J. Electron. Mater.* 45, 4237 (2016).
8. R. Arpe, H. Muller-Buschbaum, and Z. Anorg, *Allg. Chem.* 426, 1 (1976).
9. B.D. White, W.M. Patzold, and J.J. Neumeier, *Phys. Rev. B* 82, 094439 (2010).
10. K. Yoshii, T. Fukuda, H. Akahama, J. Kano, T. Kambe, and N. Ikeda, *Physica C* 471, 766 (2011).
11. V.M. Denisov, L.A. Irtyugo, L.T. Denisova, S.D. Kirik, and L.G. Chumilina, *Phys. Solid State* 54, 1943 (2012).
12. S.P. Berglund, F.F. Abdi, P. Bogdanoff, A. Chernseddine, D. Friedrich, and R. van de Krol, *Chem. Mater.* 28, 4231 (2016).
13. A.M. Abdulkarem, J.L. Li, A.A. Aref, L. Ren, E.M. Elssfah, H. Wang, Y.K. Ge, and Y. Yu, *Mater. Res. Bull.* 46, 1443 (2011).
14. Y. Xie, Y. Zhang, G. Yang, C. Liu, and J. Wang, *Mater. Lett.* 107, 291 (2013).
15. J.W. Zhang and Y.Y. Jiang, *J. Mater. Sci.-Mater. El.* 26, 4308 (2015).
16. S. Anandan, N. Pugazhenthiran, G.J. Lee, and J.J. Wu, *J. Mol. Catal. A-Chem.* 379, 112 (2013).
17. A.A. Ensafi, N. Ahmadi, and B. Rezaei, *J. Alloy. Compd.* 652, 39 (2015).
18. Y.C. Zhang, H. Yang, W.P. Wang, H.M. Zhang, R.S. Li, X.X. Wang, and R.C. Yu, *J. Alloy. Compd.* 684, 707 (2016).
19. Y. Zhang, Y. Xie, J. Li, G. Yang, T. Bai, and J. Wang, *J. Alloy. Compd.* 580, 172 (2013).
20. R. Patil, S. Kelkar, R. Naphade, and S. Ogale, *J. Mater. Chem. A* 2, 3661 (2014).
21. M. Wang, J. Zai, X. Wei, W. Chen, N. Liang, M. Xu, R. Qi, and X. Qian, *CrystEngComm* 17, 4019 (2015).
22. W.D. Oha, S.K. Lua, Z. Dong, and T.T. Lim, *Nanoscale* 8, 2046 (2016).
23. X. Chen, Y. Dai, and J. Guo, *Mater. Lett.* 161, 251 (2015).
24. S. Yuvaraj, K. Karthikeyan, D. Kalpana, and Y.S. Lee, *J. Colloid Interf. Sci.* 469, 47 (2016).
25. W.P. Wang, H. Yang, T. Xian, and J.L. Jiang, *Mater. Trans.* 53, 1586 (2012).
26. V. Vivier, A. Regis, G. Sagon, J.Y. Nedelec, L.T. Yu, and C. Cachet-Vivier, *Electrochim. Acta* 46, 907 (2001).
27. F. Wang, H. Yang, H.M. Zhang, J.Y. Su, and X.X. Wang, *J. Electron. Mater.* 46, 182 (2016).
28. A. Allagui, T. Salameh, and H. Alawadhi, *J. Electroanal. Chem.* 750, 107 (2015).
29. M. Zhu, D. Meng, C. Wang, G. Diao, and A.C.S. Appl, *Mater. Inter.* 5, 6030 (2013).
30. V. Vivier, C. Cachet-Vivier, S. Mezaille, B.L. Wu, C.S. Cha, J.Y. Nedelec, M. Fedoroff, D. Michel, and L.T. Yu, *J. Electrochem. Soc.* 147, 4252 (2000).
31. M. Aghazadeh, A.N. Golikand, and M. Ghaemi, *Int. J. Hydrogen Energy* 36, 8674 (2011).
32. M.D. Stoller, S.J. Park, Y.W. Zhu, J.H. An, and R.S. Ruoff, *Nano Lett.* 8, 3498 (2008).